ISSN 2004-2965 Energy Proceedings, Vol. 17, 2021

Paper ID APEN-MIT-2021_28
Applied Energy Symposium: MIT A+B
August 11-13, 2021 • Cambridge, USA

Radiation Damage Study of T91/Fe-Cr-Si Multimetallic Layered Composite for Generation IV Reactor Deployment

Shiddartha Paul
Department of Mechanical Engineering
The University of Alabama
Tuscaloosa, United States.
spaul11@crimson.ua.edu

Daniel Schwen
Department of Computational Mechanics and Materials
Idaho National Laboratory
Idaho Falls, United States
Daniel.Schwen@inl.gov

Micheal P. Short
Department of Nuclear Science & Engineering
Massachusetts Institute of Technology
Cambridge, United States
hereiam@mit.edu

Kasra Momeni
Department of Mechanical Engineering
The University of Alabama
Tuscaloosa, United States.
kmomeni@ua.edu

Abstract— Multimetallic layered composites (MMLC) have been explored for their suitability as nuclear fuel cladding in nuclear reactors. We studied the radiation resistance of a new MMLC, i.e., T91($Fe_{90}Cr_9Mo_1$)/Fe-Cr-Si ($Fe_{86}Cr_{12}Si_1$), for nuclear fuel cladding in Generation IV reactors, such as Molten Salt Reactor (MSR). We used a multi-objective optimization (MOO) approach to parameterizing a Modified Embedded Atom Method (MEAM) forcefield with Ziegler-Biersack-Littmark (ZBL) modification that can reproduce the two alloy's mechanical properties and perform the high energy collision cascade simulations. We performed simulations for a broad range of Primary Knock on Atom (PKA) energies, 10-100keV, at 1000K to investigate the effect of the PKA energy on the radiation damage. We found that the diffusion coefficient follows a linear trend with the radiation dose but inversely relates to PKA energies. The mean squared displacement (MSD) at the thermal spike (TS) phase is independent of the PKA energy and decreases during the ballistic phase of the cascade simulation at higher PKA energy. We revealed structural rearrangement for Fe-Cr, Si-Cr, Cr-Mo, and Mo-Mo neighboring atoms upon reaching a critical radiation dose. Our investigation also shows that the number of defects decreases as the PKA energy increases.

Keywords— Multimetallic layered Composite (MMLC), Nuclear Material, Radiation Damage, T91, Cascade Simulation, Molecular dynamics

I. INTRODUCTION

The need for new radiation-resistant materials for advanced nuclear reactors has increased over the last few decades. The high functionality of the advanced reactor requires the structural and cladding material to be intact in extreme conditions (e.g., elevated temperature, corrosive environment, and extreme radiation). Researchers have been developing nickel-based austenitic steel alloys for nuclear application [1]. Swelling the cladding material under irradiation at reactor operating temperature becomes a significant problem in advanced reactor structural and cladding applications. These Ni-based austenitic steel alloys have a maximum swelling rate of 1% per dpa when exposed to irradiation for a high transient period [2], which results in embrittlement upon a more extended period. Ferritic-martensitic (F-M) alloys are becoming a prime candidate for the advanced reactor's structural and fuel cladding application because of their high strength, radiation resistance, thermal stress resistance, and dimensional stability at extreme conditions [3], [4]. They have some unique qualities as a cladding material as they have a Body-Centered Cubic (BCC) crystal structure with a swelling rate of 0.2% per dpa [2], which is lower than the austenitic alloys. A comprehensive experimental study has investigated the microstructural evolution and mechanical properties [5]–[7]. In F-M alloys, approximately 9-12% of Cr is considered the high percentage, and the minor elements play an essential role in the phase formation [8]. Several experimental studies have been performed to describe the radiation response and microstructural change due to the radiation damage [9]–[12].

F-M alloys can develop a Cr-enriched phase near the grain boundary (GB) that causes the embrittlement of the alloy [13]. T91 alloy, an attractive candidate for nuclear fuel cladding application in generation IV advanced reactors, is an F-M alloy with 9% Cr and 1% Mo with iron that has high corrosion resistance [14] and lower swelling rate (0.09%-1.76% for 200dpa at 693K) than the other Ni-based austenitic alloys [9], [15]. In some cases, T91 alloys exhibit better swelling resistance with a more extended swelling incubation period than other F-M alloys [9].

Here, we have studied an MMLC structure of T91 and another F-M alloy ($Fe_{86}Cr_{12}Si_2$) under irradiation at a reactor

operating temperature[16], [17]. We choose $Fe_{86}Cr_{12}Si_2$ due to its excellent corrosion resistance under nuclear reactor-like environment [18], [19]. We have considered Mo and Si as those minor elements of T91. We analyzed the radiation-induced mixing through the heterostructure interface, radiation-induced defect formation, and structural disorder as a function of radiation dose. The results presented here pave the way to understand radiation-induced damage better, provide a pathway to reduce material degradation under extreme nuclear reactor-like conditions, and explore new materials that would facilitate next-generation nuclear reactors' safe, sustainable, and economical operation.

II. Computational Modeling

We have considered the T91/$Fe_{86}Cr_{12}Si_2$ MMLC heterostructure for radiation damage modeling at different PKA energies. To construct the composite structure for our simulation, we have taken a BCC lattice of Fe, which has a lattice constant of 2.866 Å. Then we have taken the 100×50×50 unit cell of Fe with 500,000 atoms. To form the T91 composite structure, we have replaced the Fe atoms from the left half of the structure with 9% and 1% of Cr and Mo atoms, respectively. To construct the Fe-Cr-Si alloy, we have replaced the Fe atoms from the right half of the lattice with the 12% and 2% of Cr and Si atoms, respectively. The heterostructure layer interface is located at the 143.3Å from each side of the structure.

We are capitalizing on our potential for Fe-Cr-Si [20] and added quaternary interactions Fe-Mo, Cr-Mo, Mo-Si, and Mo-Mo interaction to model T91. We adopted the Fe-Mo and Cr-Mo from the MEAM potential for the Fe-C-Cr-Mo system [21], and the Mo-Si interaction has been adopted from Ref. [22]. We have followed a MOO procedure to merge all these interactions [23]. In this approach, m objectives define the vector $J = [J_1(x) \dots J_m(x)]^T$, and vector x defines the individual objectives $x = [x_1 \dots x_n]^T$. Given many objectives in the 2 NN MEAM method, it is unprovable that a single set of parameters will optimize all of these objectives. Hence, a scalarization with weighting factors was included to minimize all of the elements and avoid the dominance of one, i.e., $J(x) = \sum_{i=1}^{m} w_i J_i(x)$, where w_i adjusts the effect of each parameter. Each target function is based on the differences between the obtained and target reference values, where the normalized objective vector is $J_i(x) = [(Q_i(x) - Q_i^0)/Q_i^0]^2$. Here, Q_i^0 is the reference value, and Q_i is computed by the tested potential. This process was repeated until reaching a minimum of the error value.

The data was analyzed and enhanced using the MOO process. Weighting factors were used to build a potential that regenerates elastic constants, ground-state energies, and structural characteristics. Due to a lack of a reference for the 1:1 element ratio for the Mo-Si, we used the C11b structure with a $MoSi_2$.We compared our obtained value using the fitted interaction parameters with the literature values. The comparison showed that our MEAM values are in excellent agreement with the DFT and experimental calculations, Table 1. The developed potential files are included in the supporting information.

Fig. 1(a) shows the variation of the MEAM and ZBL modified MEAM interatomic potential energy as a function of the separation distances. In our system, we have used Fe-based alloy, which has the bcc structure with a lattice constant of 2.866Å and the first nearest neighbor atom distance is 0.866a. Therefore, the inner and the outer radii in ZBL potential should be less than 2.49Å and in our case we have chosen 1.50Å and 2.00Å for inner and outer radii pairs. We have used the successive displacement cascade algorithm using the Molecular Dynamics (MD) simulation. We have initiated the process with the relaxation of the whole system at 1000K with Nose-Hoover canonical ensemble for 15 ps with a timestep of 0.001 ps before cascade collision simulation. We randomly chose the PKA at the T91 alloy on the left side to initiate cascade collision, considering the radiation source is positioned on that side. After randomly selecting the PKA, velocity was assigned equivalent to specific kinetic energy to start the high energy collisions. In our study, we have tested our MMLC system for five different values of kinetic energies, i.e., 10, 30, 50, 80, and 100keV. The velocity has been distributed in different directions, where the absolute velocity value corresponding to the kinetic energy is set to be maximum in the direction normal to the Inconel-Ni heterostructure interface, i.e., v = (0.99,0.135,0.042) |v|, so that the PKA can hit though the heterostructure interface [24]. These random values have been assigned to ensure maximum velocity in X-direction while keeping the resultant same.

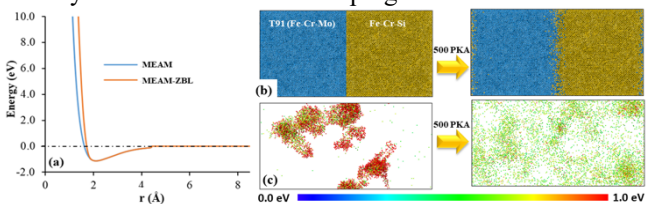

Figure 1. ZBL modified interatomic potential and structural evolution due to the radiation cascade simulation; (a) potential plots for the pure MEAM and ZBL modified MEAM potentials; (b) structural evolution from the initial structure after 500PKA simulation for 10keV energy cascade; (c) cascade formation at the first PKA initiation and after 500 PKA completion and respective cascade-energy color-coding scale.

To ensure the maximum numerical efficiency of our PKA-initiated cascade collision event, we have used a variable adaptive timestep algorithm for 10,000 steps (≈10 ps) with an NVE ensemble. Followed by this, the structure has been brought back to its initial temperature (1000K) with a Noose-Hoover thermostat to detect the defects as a result of radiation dose increment after each cascade event. This displacement cascade has gone through successive repetitions to increase the radiation, and we have performed up to 500 successive PKA events for all simulations. In Fig. 1(b), we see the evolution of the structure after introducing 500 PKA-initiated cascade events. The sharp and thin T91/Fe-Cr-Si MMLC heterostructure interface transformed to a wide interface, and the atoms mix through the interface from the T91 to Fe-Cr-Si alloy portion. Fig. 1(c) shows the cascade formation during the initial and the final PKA and their evolution as the simulation proceeds. We can see that, at the initial cascade, few atoms were energized by the initial PKA, and as the simulation went on, a large number of the atoms were energized by successive cascade events. As the subsequent simulation process proceeded, the canter of mass of the structure was continuously shifting. Therefore, we had to balance the linear and the angular momentum for unwanted shifting of the particles through

the periodic boundaries. All these simulations have been carried out by the Large-scale Atomic/Molecular Massively Parallel Simulator (LAMMPS) open-source code [25]. We have reached a damage level of 0.7-1.3 dpa depending on the PKA energy. The number of the PKAs introduced in the cascade simulation was fixed, but the energy per PKA (E_{PKA}) is different for each PKA energy case. The damage level we have achieved is very different than the experimental, where several hundreds of nanometer depths need to be analyzed for radiation damage. The PKA energized several MeV of PKA energy in experiments [26]. However, it has been seen from the energy spectrum that most of the atoms absorb 10 KeV-1.5MeV energy[26]. Our simulation study used 10–100 keV with a reasonably dimensioned atomic system to ensure maximum computational efficiency and reach a damage level comparable to the experimental damage study[27].

Table 1. Mo-Si2 properties comparison before and after the potential fitting.

MoSi2 *C11b*	Cohesive Energy (E_v)	a/c lattice (Å)	Elastic constants (GPA)			Shear Modulus (GPA)	Young Modulus (GPA)	Bulk Modulus (GPA)	Poisson's Ratio
	E_c	*alat*	C_{11}	C_{12}	C_{44}	*G*	*E*	*B*	*v*
No fit MEAM	-5.66	3.46/8.80	242.73	156.82	42.31	84.83	225.37	218.93	0.33
Our fitted MEAM	-5.65	3.11/9.55	396.52	116.16	173.55	158.70	385.09	223.86	0.21
MEAM [22]	-5.92	3.59/8.42	252.00	145.00	26.00	75.00	202.00		0.34
DFT [28]	-23.19	3.22/7.87						203.70	
DFT [29]		3.18/7.79	406.4	111.5	202.1			211.6	
Exp. [30]		3.20/7.85	410.00	114.90	195.00				
Exp. [31]	-19.14	2.446	401.00	102.00	208.00			222.00	

We have used the Stopping and Range of Ions in Matter (SRIM) code to determine the E_{PKA}. For SRIM calculations, we have set up a system similar to our MD simulation structural condition. In Fig. 2, the calculated damage level or radiation dose per E_{PKA} has been plotted as a function of PKA energy. We revealed a plateau in saturation trend comes as the PKA energy increases.

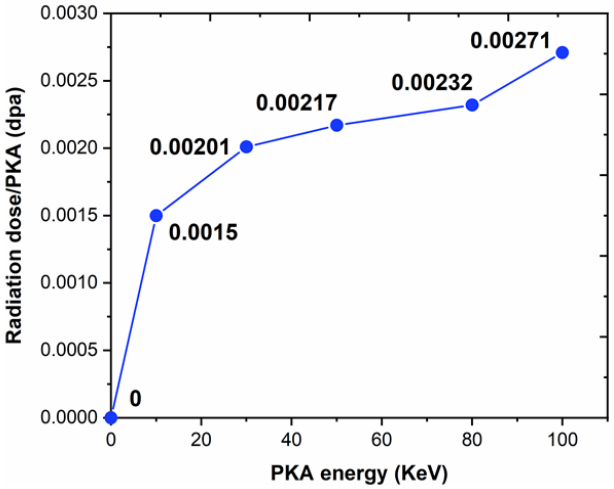

Figure 2. Calculation of radiation damage level using SRIM code for different PKA energies.

As the PKA energy increases, the kinetic energy of the atoms upon collision increases, leading to more significant damage to materials. According to the following expression, this energy distribution becomes almost the same for the PKAs with increasing energy due to their dependence on the recoil cross-sections [32].

$$dpa_{ij}\ rate = \frac{0.8}{2E_d}\sum_n \phi_n \sum_k m_{kn}^{ij}\, T_j^k \quad (1)$$

Here ϕ_n is the particle flux used to calculate the PKA distributions associated with E_{PKA}; E_d is the threshold displacement energy or the energy required to produce Frenkel pair atomic defects in the lattice. The recoil energy cross-sections are defined via the energy bins (e.g., n or k bins), m_{kn}^{ij} is the cross-section in the barn for recoil energy of group k incident on the target neutron with an energy group n for a reaction $i \rightarrow j$, and T_j^k is the damage energy associated with incident neutron j with PKA energy k.

III. Results and Discussion

We revealed the formation of cascades leading to radiation-induced segregation, void formation, defect accumulation, and other physical and mechanical effects. The cascade events evolve in several periodic stages, i.e., initial collision, TS region, quenching phase, and the annealing phase. In the collision stage, the primary knock-on atom initiates the displacement cascade, which lasts until the creation of further displacements or energy dissipation. This stage ends in a very short period (<<1ps), and the displaced atoms in the lattice sites do not have enough time to form defects. Following the collision stage, the TS region starts, which its development requires ~0.1-0.15ps, and the maximum cascade energy dissipate to the neighboring atoms within ~1.0-1.5 ps. After dissipating the kinetic energy to the surrounding atoms, the ballistic phase emerges. The ballistic phase (~9ps) is crucial for defect diffusion and annihilation, leading to tractable damage. The TS region in each cascade

event is crucial as radiation-induced segregation is maximum at this stage. Fig. 3(a) and (b) show the MSD as a function of simulation time for 10keV and 100keV, respectively, revealing comparable MSD values at the TS region for 10 keV and 100keV. However, at the end of the cascade, the MSD increases slowly for 10 keV during the ballistic phase of the cascade, while it decreases for 100 keV.

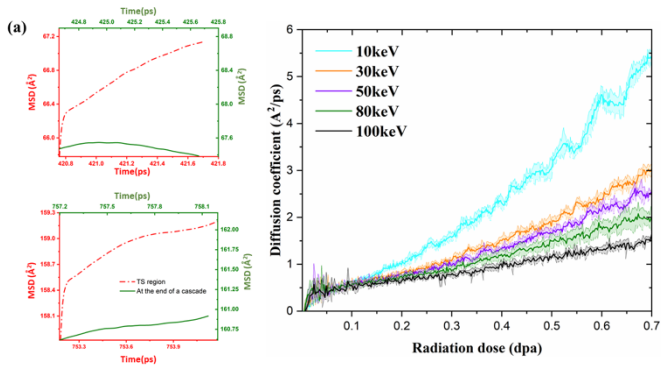

Figure 3. Mean squared displacement for (a) 10KeV and (b) 100KeV PKA at the very initial cascade; (c) radiation enhanced diffusion for different cases and time of the simulation.

Fig. 3(c) represents the radiation enhanced diffusion (RED) coefficient variation for our system with different E_{PKA} as a function of radiation dose, indicating an increasing linear trend of the RED with the radiation dose. The RED for 10 keV is much higher than for other E_{PKA}. Furthermore, Fig. 3(c) shows that the RED coefficient decreases as the E_{PKA} increases. The difference between the RED coefficient for different E_{PKA} increases as the radiation dose increases. The diffusion coefficient has been calculated using Einstein relation[33], $D = \frac{<r_s^2(t)>}{2nt}$. Here $< r_s^2(t) >$ is the MSDof particles, s determined over time, t, in a system with n dimensions. In our simulations, n=3, as we have a 3D material system. The MSD has been calculated using this expression $MSD = \frac{1}{N}\sum_{i=1}^{N} < |r(t) - r(0)|^2 >$; here N is the number of atoms in our system and i is the atom id. The RED value has been determined for the diffusion of all the atoms rather than the selective ones because of their close radiation responsiveness. RED occurs mainly due to the vacancy or defect formation during the radiation. As the radiation-induced vacancy concentration is higher than the thermally produced vacancy, the value of RED is much higher than the thermally induced self-diffusion coefficient. That is why we have got a higher RED coefficient in a range of 10^{-9}-10^{-8} m^2/s than the thermally induced self-diffusion coefficient (10^{-17}-10^{-19} m^2/s) [34]. Our RED coefficient findings agree with the previous study for Fe-Cr-based alloy irradiation [35]. This radiation-enhanced diffusion and defect formation widen the MMLC's heterostructure interface, Figs. 1(b) and 4(a). The interfacial thickness increases exponentially with the radiation dose initially and reaches a plateau as the radiation dose increases, Fig. 4(a). Furthermore, Fig. 4(b) and (c) represent the atomic mixing through the MMLC structure for different radiation doses of 10keV-100keV. It can be visually observed that the atomic mixing is a bit higher for 100keV than it is for 10keV. However, in those mixing through the structure plots, we see that the atomic mixing tendency for different radiation doses gets saturates after 0.2 dpa (the mixing curves are very close to each other when radiation dose > 0.2dpa, Fig. 4(a) and (b). That is why we see a less dependence of interface thickness on radiation dose after 0.2 dpa which results in the saturation of interface thickness, Fig. 4(a).

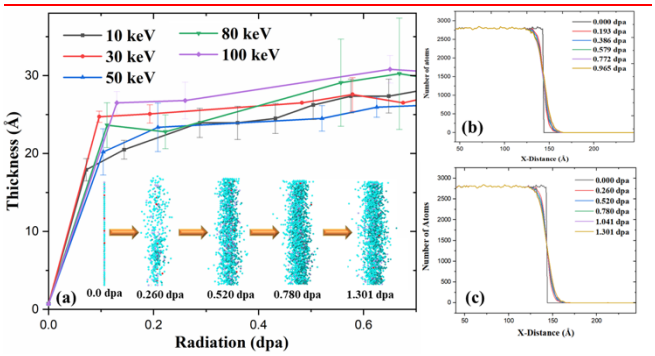

Figure 4. Radiation-induced mixing through T91/FeCrSi interface, (a) interfacial thickness; elemental mixing with (b) 10KeV and (c) 100KeV PKA.

In Fig. 5, the defect density as a function of radiation dose in the T91/ Fe-12Cr-2Si MMLC system has been presented for different E_{PKA}. The radiation-induced vacancies and interstitials accumulated due to the repetitive collision of high-energy particles and atoms. Formation of interstitial and vacancy is a simultaneous process, and these vacancy-interstitial pairs are known as Frenkel pairs (FP). During the radiation, the density of defects produced during the cascade may alter by the annihilation or the recombination of the vacancy or interstitials. Fig. 5(a) shows that the density of FP increases at higher radiation doses and upon increasing the E_{PKA}.

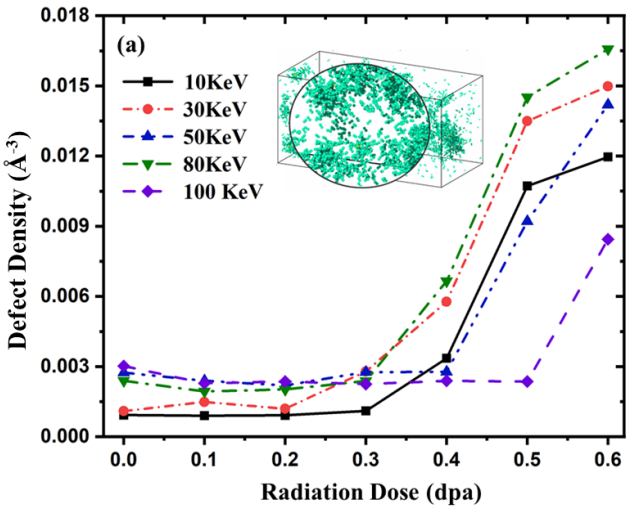

Figure 5. Defect density in the T91/ Fe-12Cr-2Si MMLC. The density of defects remains almost constant at low radiation doses and increases when the radiation dose passes a critical value that is a function of E_{PKA}

Fig. 6(a) plots the pair correlation at the initial collision cascade, showing the lack of the long-range order in mutual pair of atoms as the atoms are sparsely distributed over a wide range of bond length. Fig. 6(b) revealed an increase in the peak value of Cr-Si, Mo-Mo, Cr-Mo, and Si-Si upon irradiation, indicating domination of their preferred nearest distance upon irradiation that can be due to the better mixing of these elements through the sample. In the case of the Mo-Mo radial distribution function, we revealed a loss of long-

range order upon irradiations indicated by the almost constant nonzero g(r) value. Coordination analysis also indicates the enrichment of the Cr-associated phase, possibly increasing the hardness of the microstructure [36] and saturating the radiation damage, as we have seen earlier from our results and literature discussions. However, such formation of Cr enriched phases near grain boundaries leads to embrittlement of the material.

IV. Conclusions

We studied the radiation damage for an MMLC system consisting of T91/ Fe-12Cr-2Si alloys irradiated at different E_{PKA}. Our simulations indicate that the diffusion coefficient follows a linear trend with the radiation dose and inversely relates to E_{PKA}. Most of the PKA energy absorbed during the TS stage and the radiation-enhanced MSD during the TS stage is higher than each cascade's ballistic phase. Furthermore, the MSD is the same at the TS phase for different PKA energies. However, at higher PKA energy, a decreasing trend of MSD has been seen in the ballistic phase of a cascade simulation.

Using coordination analysis, we revealed a structural rearrangement for Fe-Cr, Si-Cr, Cr-Mo, and Mo-Mo, indicating the Cr enrichments near the GBs, which has also been reported experimentally [37], [38]. We also realized that increasing radiation dose widens the sharp interface as the defects and the interstitials diffuse through the interface. The thickness of the interface curves becomes saturated as the radiation increases beyond 0.2dpa due to Cr enrichment in the GBs of the T91/Fe-12Cr-2Si MMLC system. Moreover, the defects for different E_{PKA} also plateau as the radiation goes beyond the 0.2 dpa. The recombination rate is also lower at higher radiation doses due to the lower sink efficiency due to structural alternation GBs. Our results revealed a dynamic relationship of radiation damage quantities, e.g., radiation defect, interfacial thickness, RED, and radiation-induced mixing with radiation dose for this particular MMLC system, consistent with experimental reports[37], [38].

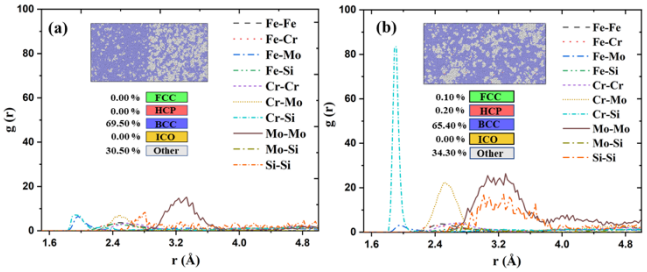

Figure 6. Structural coordination analysis of different elements; (a) the initial structure with 0.0 dpa, and (b) the final structure after 1.0 dpa with common neighbor analysis for respective structure.

Acknowledgment

This project is partly supported by DoE-ARPA-E OPEN (DE-AR0001066) and the NSF-CAREER under NSF cooperative agreement CBET-2042683.

References

[1] F. A. Garner, "4.02 Radiation damage in austenitic steels," *Compr. Nucl. Mater.*, vol. 4, pp. 33–95, 2012.

[2] F. . Garner, M. . Toloczko, and B. . Sencer, "Comparison of swelling and irradiation creep behavior of fcc-austenitic and bcc-ferritic/martensitic alloys at high neutron exposure," *J. Nucl. Mater.*, vol. 276, no. 1–3, pp. 123–142, Jan. 2000, doi: 10.1016/S0022-3115(99)00225-1.

[3] S. Jitsukawa *et al.*, "Development of an extensive database of mechanical and physical properties for reduced-activation martensitic steel F82H," *J. Nucl. Mater.*, vol. 307–311, pp. 179–186, Dec. 2002, doi: 10.1016/S0022-3115(02)01075-9.

[4] A. Kostka, "On the contribution of carbides and micrograin boundaries to the creep strength of tempered martensite ferritic steels," vol. 55, pp. 539–550, 2007, doi: 10.1016/j.actamat.2006.08.046.

[5] S. J. Zinkle, "1.03-Radiation-Induced effects on microstructure," *Compr. Nucl. Mater.*, vol. 1, pp. 65–98, 2012.

[6] A. Hasegawa, M. Fukuda, K. Yabuuchi, and S. Nogami, "Neutron irradiation effects on the microstructural development of tungsten and tungsten alloys," *J. Nucl. Mater.*, vol. 471, pp. 175–183, 2016, doi: https://doi.org/10.1016/j.jnucmat.2015.10.047.

[7] F. A. Garner, M. L. Hamilton, N. F. Panayotou, and G. D. Johnson, "The microstructural origins of yield strength changes in aisi 316 during fission or fusion irradiation," *J. Nucl. Mater.*, vol. 104, pp. 803–807, 1981, doi: https://doi.org/10.1016/0022-3115(82)90698-5.

[8] R. L. Klueh and D. R. Harries, "High-chromium ferritic and martensitic steels for nuclear applications," 2001.

[9] J. G. Gigax *et al.*, "Radiation response of alloy T91 at damage levels up to 1000 peak dpa," *J. Nucl. Mater.*, vol. 482, pp. 257–265, 2016.

[10] R. L. Klueh, J.-J. Kai, and D. J. Alexander, "Microstructure-mechanical properties correlation of irradiated conventional and reduced-activation martensitic steels," *J. Nucl. Mater.*, vol. 225, pp. 175–186, 1995.

[11] S. Taller, Z. Jiao, K. Field, and G. S. Was, "Emulation of fast reactor irradiated T91 using dual ion beam irradiation," *J. Nucl. Mater.*, vol. 527, p. 151831, 2019.

[12] A. Dutta *et al.*, "An approach in the analysis of microstructure of proton irradiated T91 through XRDLPA using synchrotron and laboratory source," *J. Nucl. Mater.*, vol. 514, pp. 161–170, 2019.

[13] G. S. Was, *Fundamentals of radiation materials science: metals and alloys*. springer, 2016.

[14] D. Song *et al.*, "Corrosion behavior and mechanism of Cr--Mo alloyed steel: Role of ferrite/bainite duplex microstructure," *J. Alloys Compd.*, vol. 809, p. 151787, 2019.

[15] D. S. Gelles, "Microstructural examination of commercial ferritic alloys at 200 dpa," *J. Nucl. Mater.*, vol. 233, pp. 293–298, 1996.

[16] S. Paul, D. Schwen, M. Short, and K. Momeni, "Effect of Irradiation on Ni-Inconel/Incoloy Heterostructures in Multimetallic Layered Composites," *J. Nucl. Mater.*, p. 152778, 2021, doi: https://doi.org/10.1016/j.jnucmat.2021.152778.

[17] R. R. Romatoski and L. W. Hu, "Fluoride-Salt-Cooled High-Temperature Test Reactor Thermal-Hydraulic Licensing and Uncertainty Propagation Analysis," *Nucl. Technol.*, vol. 205, no. 11, pp. 1495–1512, Nov. 2019, doi: 10.1080/00295450.2019.1610686.

[18] M. P. Short, R. G. Ballinger, and H. E. Hänninen, "Corrosion resistance of alloys F91 and Fe – 12Cr – 2Si in lead – bismuth eutectic up to 715 ° C," *J. Nucl. Mater.*, vol. 434, no. 1–3, pp. 259–281, 2013, doi: 10.1016/j.jnucmat.2012.11.010.

[19] R. G. Ballinger, "Effects of Chromium and Silicon on Corrosion of Iron Alloys in Lead-Bismuth Eutectic Effects of Chromium and Silicon on Corrosion of Iron Alloys," 2007.

[20] S. Paul, M. Muralles, D. Schwen, M. Short, and K. Momeni, "A Modified Embedded-Atom Potential for Fe-Cr-Si Alloys," *J. Phys. Chem. C*, vol. 125, no. 41, pp. 22863–22871, Oct. 2021, doi: 10.1021/acs.jpcc.1c07021.

[21] H.-L. Chen, C.-H. Su, S.-P. Ju, S.-H. Liu, and H.-T. Chen, "Local structural evolution of Fe54C18Cr16Mo12 bulk metallic glass during tensile deformation and a temperature elevation process: a molecular dynamics study," *RSC Adv.*, vol. 5, no. 126, pp. 103925–103935, 2015, doi: 10.1039/C5RA18168B.

[22] M. I. Baskes, "Atomistic potentials for the molybdenum--silicon

system," *Mater. Sci. Eng. A*, vol. 261, no. 1–2, pp. 165–168, 1999.

[23] J. Houze *et al.*, "A multi-objective optimization procedure to develop modified-embedded-atom-method potentials: an application to magnesium," *arXiv Prepr. arXiv0708.0075*, 2007.

[24] B. Xian-Ming, V. A. F., H. R. G., N. Michael, and U. B. P., "Efficient Annealing of Radiation Damage Near Grain Boundaries via Interstitial Emission," *Science (80-.).*, vol. 327, no. 5973, pp. 1631–1634, Mar. 2010, doi: 10.1126/science.1183723.

[25] S. Plimpton, P. Crozier, and A. Thompson, "LAMMPS-large-scale atomic/molecular massively parallel simulator," *Sandia Natl. Lab.*, vol. 18, p. 43, 2007.

[26] M. W. Ullah, Y. Zhang, N. Sellami, A. Debelle, H. Bei, and W. J. Weber, "Evolution of irradiation-induced strain in an equiatomic NiFe alloy," *Scr. Mater.*, vol. 140, pp. 35–39, 2017, doi: 10.1016/j.scriptamat.2017.06.042.

[27] Z. Zhu, H. Huang, O. Muránsky, J. Liu, Z. Zhu, and Y. Huang, "On the irradiation tolerance of nano-grained Ni–Mo–Cr alloy: 1 MeV He+ irradiation experiment," *J. Nucl. Mater.*, vol. 544, p. 152694, 2021, doi: https://doi.org/10.1016/j.jnucmat.2020.152694.

[28] X. P. Li, S. P. Sun, H. J. Wang, W. N. Lei, Y. Jiang, and D. Q. Yi, "Electronic structure and point defect concentrations of C11b MoSi2 by first-principles calculations," *J. Alloys Compd.*, vol. 605, pp. 45–50, 2014.

[29] X. Guo-Liang, C. Jing-Dong, X. Yao-Zheng, L. Xue-Feng, L. Yu-Fang, and Z. Xian-Zhou, "First-principles calculations of elastic and thermal properties of lanthanum hexaboride," *Chinese Phys. Lett.*, vol. 26, no. 5, p. 56201, 2009.

[30] K. Tanaka, H. Onome, H. Inui, M. Yamaguchi, and M. Koiwa, "Single-crystal elastic constants of MoSi2 with the C11b structure," *Mater. Sci. Eng. A*, vol. 239, pp. 188–194, 1997.

[31] M. Alouani, R. C. Albers, and M. Methfessel, "Calculated elastic constants and structural properties of Mo and ${\mathrm{MoSi}}_{2}$," *Phys. Rev. B*, vol. 43, no. 8, pp. 6500–6509, Mar. 1991, doi: 10.1103/PhysRevB.43.6500.

[32] M. R. Gilbert and J. C. Sublet, "Differential dpa calculations with SPECTRA-PKA," *J. Nucl. Mater.*, vol. 504, pp. 101–108, 2018, doi: 10.1016/j.jnucmat.2018.03.032.

[33] J. A. Given and B. B. Mandelbrot, "Diffusion on fractal lattices and the fractal Einstein relation," *J. Phys. A. Math. Gen.*, vol. 16, no. 15, pp. L565–L569, Oct. 1983, doi: 10.1088/0305-4470/16/15/003.

[34] H. Wen and C. H. Woo, "Quantum statistics in the spin-lattice dynamics simulation of formation and migration of mono-vacancy in BCC iron," *J. Nucl. Mater.*, vol. 470, pp. 102–110, 2016, doi: 10.1016/j.jnucmat.2015.12.005.

[35] O. Senninger, F. Soisson, E. Martínez, and M. Nastar, "Acta Materialia Modeling radiation induced segregation in iron – chromium alloys," *Acta Mater.*, vol. 103, pp. 1–11, 2016, doi: 10.1016/j.actamat.2015.09.058.

[36] G. S. Was *et al.*, "Assessment of radiation-induced segregation mechanisms in austenitic and ferritic--martensitic alloys," *J. Nucl. Mater.*, vol. 411, no. 1–3, pp. 41–50, 2011.

[37] V. Kuksenko, C. Pareige, and P. Pareige, "Intra granular precipitation and grain boundary segregation under neutron irradiation in a low purity Fe–Cr based alloy," *J. Nucl. Mater.*, vol. 425, no. 1, pp. 125–129, 2012, doi: https://doi.org/10.1016/j.jnucmat.2011.10.031.

[38] V. Kuksenko, C. Pareige, C. Genevois, F. Cuvilly, M. Roussel, and P. Pareige, “Effect of neutron-irradiation on the microstructure of a Fe–12at.%Cr alloy,” *J. Nucl. Mater.*, vol. 415, no. 1, pp. 61–66, 2011, doi: https://doi.org/10.1016/j.jnucmat.2011.05.042.